



ELSEVIER

Available online at www.sciencedirect.com

SCIENCE @ DIRECT®

Nuclear Instruments and Methods in Physics Research A 513 (2003) 473–483

NUCLEAR
INSTRUMENTS
& METHODS
IN PHYSICS
RESEARCH
Section A

www.elsevier.com/locate/nima

Two-dimensional GEM imaging detector with delay-line readout

G.P. Guedes^{a,1}, A. Breskin^a, R. Chechik^{a,*}, D. Vartsky^b, D. Bar^b,
A.F. Barbosa^c, P.R.B. Marinho^c

^aDepartment of Particle Physics, Weizmann Institute of Science, Rehovot 76100, Israel

^bSoreq NRC, Yavneh, Israel

^cCentro Brasileiro de Pesquisas Fisicas, CBPF, Rua Dr. Xavier Sigaud, 150-22290-180, Rio de Janeiro/RJ, Brazil

Received 6 February 2003; received in revised form 20 May 2003; accepted 20 May 2003

Abstract

A $100 \times 100 \text{ mm}^2$ 2D imaging detector, based on a triple-GEM gaseous multiplier, striped $x - y$ readout anode and discrete delay-line readout, is presented. The fast (2.1 ns tap^{-1}) delay-line circuit was designed to match the anode-charge signal profile, namely its rise-time and length. The detector's imaging capability was systematically studied in Ar/CO₂ (70/30) with 5.9 keV X-rays; $x - y$ resolution of $\sigma = 0.05$ and 0.1 mm for top and bottom anode strips, respectively, and integral non-linearity of $\sim 0.15\%$ are demonstrated.

© 2003 Elsevier B.V. All rights reserved.

PACS: 84.30.-r; 84.30.Bv; 29.40.Cs; 29.40.Gx

Keywords: GEM; Gaseous imaging detector; Delay-line readout; 2D readout

1. Introduction

The introduction of the Gas Electron Multiplier (GEM) [1] opened a new trend in gas detector studies. Due to its reliability and ease of operation, GEM-based detectors have become an interesting alternative for radiation detection and imaging. By applying suitable potentials on the GEM electrodes, one can reach gains in excess of 10^3 with a

single GEM foil; multiple GEMs can be assembled in cascade to provide orders of magnitude higher gains [2,3]. Several studies have shown the influence of the geometrical operation parameters of GEMs on the electron transfer processes [2,4–6] and on the spatial distribution of the avalanche-induced charges on the anode readout circuit [7–10].

Large area ($31 \times 31 \text{ cm}^2$) multi-GEM detectors have been designed for tracking in intense particle beams [10–13] and for X-ray imaging [7,14,15]; different anode geometries have been used for electron collection and 2D localization, e.g. orthogonal and small-angle strips, hexagonal pads [7,8,10,11,13–15]. Most of the readout techniques

*Corresponding author. Tel.: +972-8-9344966; fax: +972-8-9342611.

E-mail address: rachel.chechik@weizmann.ac.il (R. Chechik).

¹On leave from the Lab. for Nucl. Instrum., COPPE/UFRJ 21945-970, Cidade Universitária/RJ, Brazil.

employ large number of discrete amplifiers and shaping electronics using ASIC chips, e.g. HELIX 128 [11] and PREMUX [7]. These solutions are expensive and the chips are in general spark-sensitive; they require powerful hardware, e.g. time consuming analog multiplexing, analog-to-digital conversions and computing analysis. A simpler solution, widely employed for the readout of wire chambers, is the use of discrete delay-line position encoding [16,17]. These are discrete LC filter-cells connected to individual cathode or anode strips or wires, running at orthogonal directions. The delay-lines are read by current amplifiers, one at each end of the line; the charge localization is derived from the propagation time of the induced signal traveling along the delay-line.

In this work we present the results of laboratory studies of a $10 \times 10 \text{ cm}^2$ triple-GEM detector equipped with a newly designed 2D position encoding delay-line readout. We describe the three-GEM detector and provide its general properties and imaging performance under operation with 5.9 keV X-rays in atmospheric Ar/CO₂ (70/30).

2. The detector

The three-GEM detector is shown schematically in Fig. 1. It was assembled in a modular way, using CERN-made elements² and other homemade G-10 frames. Fig. 1a shows a top view of the open detector; Fig. 1b shows the frame arrangement and Fig. 1c shows details of the detector's active elements assembly. All the detector elements are mounted, with screws, on a base-plate, which carries the high voltage (HV) connectors and the gas inlets. The delay-line printed circuit boards (PCBs) and the base-frame are glued onto the base-plate. The window frame, with 6 μm thick Mylar, is connected to the base-frame with screws through the intermediate frame and the gas enclosure is sealed with two rubber O-rings. The detector elements comprise a stainless steel drift-cathode mesh, three $10 \times 10 \text{ cm}^2$ GEMs stretched

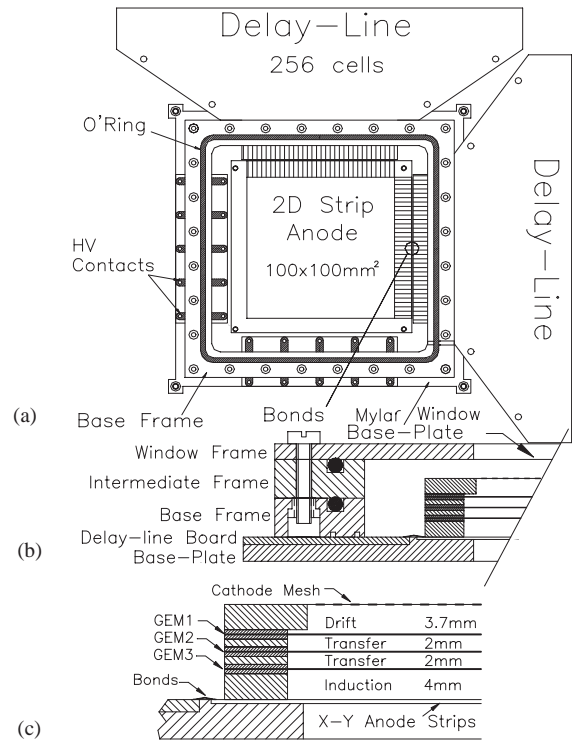


Fig. 1. Details of the 2D three-GEM detector assembly: (a) top view of open detector; (b) side view showing frames arrangement and (c) detailed side view. All the frames and spacers are made of G-10.

on 0.5 mm-thick G-10 frames and the 2D strip-anode with connecting pads, which are bonded to the delay-line pads on PCBs by 200 μm wide gold ribbons. The GEMs, made at CERN, have bi-conical holes, 60 μm diameter at the Kapton and 80 μm diameter at the metal faces; they are arranged in a hexagonal pattern with a pitch of 140 μm . The 2D anode-strip electrode is made of two orthogonal strip-layers, separated by 50 μm thick Kapton and glued on a 0.5 mm G-10 support. Each layer has 512 gold-coated strips, 200- μm pitch; the top- and bottom-layer strips are 80 and 150 μm wide, respectively. This geometry results in a charge ratio (top-to-bottom) of 2:1 [10]. The drift, transfer and induction gaps, defined by spacers, are 3.7, 2 and 4 mm, respectively.

From our recent measurements [9] of avalanche-induced electron-cloud lateral distributions in an Ar/CO₂ (70/30) operated double-GEM detector,

²A modular GEM detector system designed by F. Sauli, CERN, Geneva.

we can calculate the expected lateral distribution in the three-GEM configuration. It is slightly further enlarged by electron diffusion in the additional, 2 mm wide, transfer gap. Thus, the expected lateral distribution of the electron cloud at the anode has a sigma of about 230 μm ; this is broad enough to allow for interconnecting every two anode strips into a single delay-line cell, resulting in 256 cells at 400 μm steps, per each dimension. The delay-line PCB was designed as a compact, double-sided circuit. Its components are located outside the detector whereas the bonding of the delay-line PCB to the anode strips is located inside the detector volume.

The GEMs are powered with a resistor network and a single negative power supply, as discussed in Chapter 4, in order to protect the detector against occasional discharges. The resistors values were chosen to provide a voltage drop across each GEM of $V_{\text{GEM}} = 425 \text{ V}$ and fields of $E_{\text{D}} = 1150 \text{ V cm}^{-1}$, $E_{\text{T}} = 2100 \text{ V cm}^{-1}$ and $E_{\text{I}} = 2700 \text{ V cm}^{-1}$ for the drift, transfer and induction gaps, respectively.

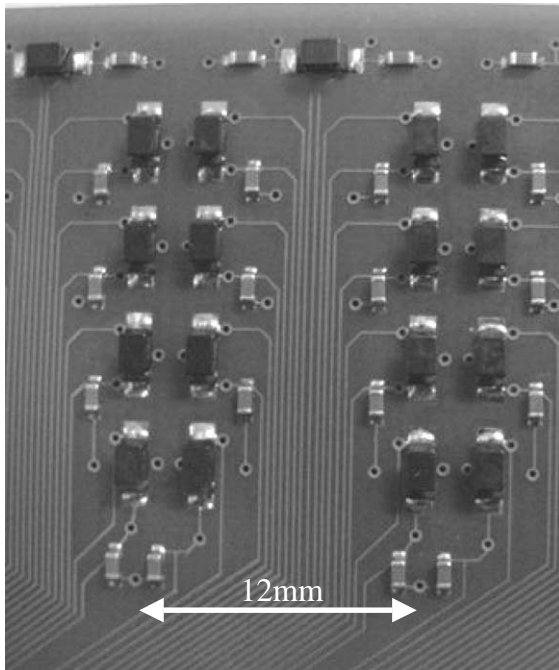


Fig. 2. A photograph of a segment of the delay-line circuit, highlighting its undulating structure on top.

3. The delay line

Discrete-element delay-lines have been widely used to identify the position of ionizing events in gaseous detectors. Our goal was to show the viability of delay-lines as a cost effective 2D readout solution in association with a $100 \times 100 \text{ mm}^2$ triple-GEM detector having a readout anode with orthogonal strips (400 μm readout pitch). Using very small surface mounted devices (SMD) we designed a delay-line with 256 LC cells; its parameters were chosen according to the following requirements: (i) high impedance $Z = \sqrt{L/C}$, (ii) small size, (iii) low intrinsic inductor resistance R_i , (iv) tight tolerance and (v) good thermal stability. Except for the first, all requirements are related to the components manufacturing quality and technology.

We have chosen wire-wound inductor coil on ferrite core ($L = 290 \pm 5\% \text{ nH}$) with nominal DC resistance $R_i = 0.17 \pm 3\%$ and monolithic ceramic capacitors ($C = 6.8 \pm 0.25 \text{ pF}$), both from Murata.³ The respective element sizes for the inductor and the capacitor are $3.2 \times 1.6 \text{ mm}^2$ (standard 1206) and $1.6 \times 0.8 \text{ mm}^2$ (standard 0603). With these components we calculated the delay per tap to be 1.4 ns, the line impedance to be 206Ω and the total DC resistance of a 256-cells line 43Ω . The delay-line elements are arranged in an undulating line over $24 \times 4 \text{ cm}^2$ area on both sides of the PCB, each LC cell having neighbors on the opposite side of the PCB (Fig. 2).

Based on this PCB delay-line, and using our previously measured rise-time and pulse width of the induced signal on the readout circuit [9], we have simulated, and tested the performance of a 256-cell circuit, as detailed in the next sections.

3.1. Measurement and simulation results

The performance of the delay-line circuit in terms of amplitude attenuation and rise-time variation along the line was measured prior to its bonding to the anode strips and was compared to the simulated performance. The experimental arrangement is shown in Fig. 3. The 220Ω resistive

³<http://www.murata.com/>

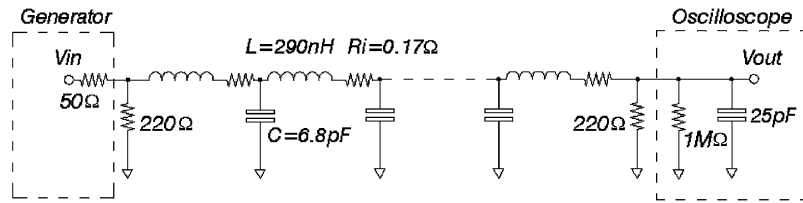


Fig. 3. Equivalent LRC circuit of the delay-line prior to its bonding. It represents the actual inductor as a non-resistive coil (L) in series with an internal resistance (R_i). In this case the delay-line is terminated resistively (R_t) with a capacitive decoupling.

termination was found to be the best value to minimize the reflections.

Based on previous experiments of anode signal time development [9], and considering the detector induction parameters (gap and field), we decided to use in both the simulations and the measurements a ‘square’ input signal with 7.5 ns rise-time and 100 ns width. We injected a signal to one extremity and recorded the delayed pulses along the delay-line cells. Fig. 4 shows the input pulse and its delayed output recorded from the delay line PCB. The total delay measured was about 380 ns (1.5 ns cell^{-1}), slightly above the calculated value of 1.4 ns cell^{-1} . This difference may be explained by the presence of some parasitic capacitance increasing the effective values of C , therefore increasing the total delay.

We used the program ORCAD⁴ PSpice Version 9.0 to simulate the delay-line circuit response. In the simulation we have also taken into account the parameters of the pulse-generator (output impedance 50Ω), used on the test bench to provide the input signal, and that of the oscilloscope, used to observe the output signal (input impedance $1 \text{ M}\Omega$; capacitance 25 pF). The simulated circuit, shown in Fig. 3, reproduces the experimental setup. Due to the large number of inductors, we were particularly interested in the effect of their resistivity on the signal attenuation and rise-time degradation along the delay-line cells. We have therefore studied two cases: a delay-line with intrinsic nominal resistivity ($R_i = 0.17 \pm 3\% \Omega$) and without resistivity ($R_i = 0 \Omega$) for comparison.

Fig. 5 shows the measured and simulated amplitude attenuation along the delay-line. The discrepancy between simulated ($R_i = 0.17 \Omega$) and

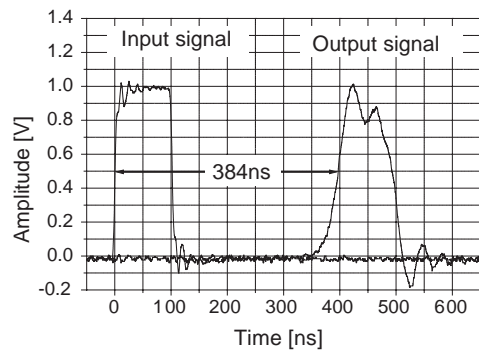


Fig. 4. The input square pulse with 7.5 ns rise-time, 100 ns width and 1 V amplitude (left) used in the delay line evaluation measurements and the output pulse, delayed by 384 ns, after 256 cells.

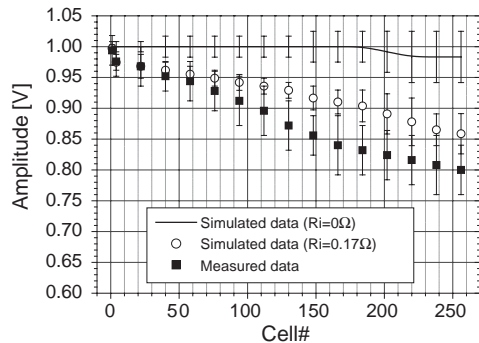


Fig. 5. Simulated and measured amplitude attenuation along the delay-line prior to its bonding for a square input pulse (see Fig. 4). The simulations were done for both non-resistive (open circle) and for the maximum nominal intrinsic resistance (closed triangle) of the inductor.

measured data is about 7%. The maximum attenuation is 20%, which is generally acceptable. Fig. 6 shows the measured and simulated rise-time (from 10% to 90% of maximum amplitude)

⁴<http://www.orcad.com/>

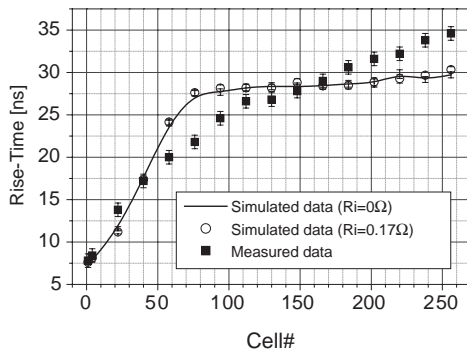


Fig. 6. Simulated and measured rise-time variation, (10–90% of maximum) along the delay-line prior to its bonding, for a 7.5 ns rise-time and 100 ns wide square input pulse. The simulated data show no dependence on the assumed intrinsic resistance of the inductor.

variation along the delay-line. It is clear from the simulation that the rise-time variation is not sensitive to the inductors resistance and it increases from 7.5 up to 30 ns. The rise-time recorded experimentally increases monotonously along the line, reaching 35 ns at the delay-line end. The difference between simulated and experimental data could be due to the parasitic capacitance on the parallel strips connecting the delay-line cells to the PCB edge, which was not included in the simulations. This parasitic capacitance acts as a feedback capacitor, which affects the delay-line time response: it allows for higher frequencies to be transmitted and actually improves the linearity between rise-time and delay-line length. The mutual inductance between neighboring inductors could also affect the time response and should be considered in the simulation, but it is very difficult to estimate its value.

3.2. Delay-line coupled to the detector

The delay-line circuit is placed outside the detector volume; it has connecting strips (400 μm pitch), each bonded to two anode strips (the anode has a 200 μm pitch) with 200 μm wide and 25 μm thick gold ribbons. After bonding the delay-line to the anode strips, parasitic capacitances between neighboring strips and between the strip planes, of about 3.1 and 8.5 pF, respectively [7], modified the

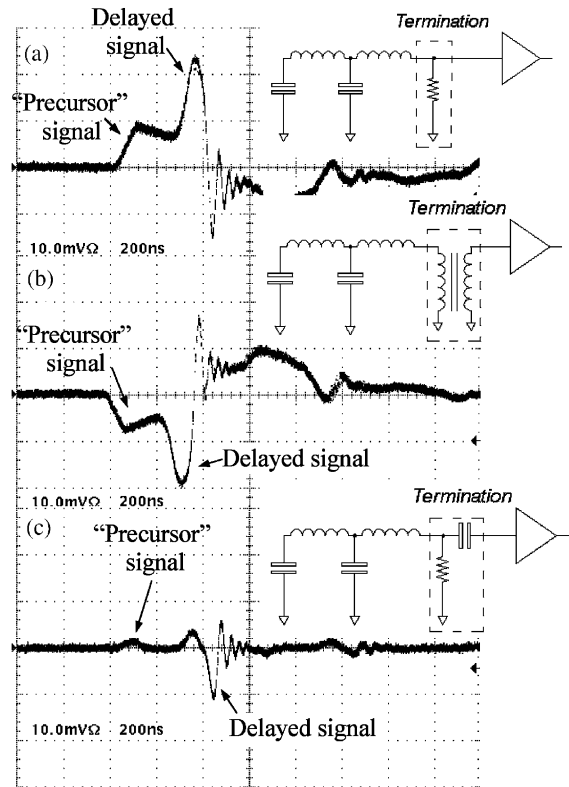


Fig. 7. Results of tests carried out with the GEM detector and three delay-line termination types: (a) resistive, (b) inductive and (c) capacitive. In the first two, we observe a broad precursor signal; it is largely reduced by using a capacitive termination (c), finally used in the detector.

delay-line AC characteristics; the total delay increased by about 50% compared to the designed value, namely from 360 ns to about 540 ns. The signals are read at both ends of the line with a fast preamplifier, via impedance-matching termination.

The termination should match the delay-line impedance of $Z = 206 \Omega$ to the external-electronics impedance of 50Ω , and avoid reflections along the delay-line circuit. Using the output signal generated by a collimated ^{55}Fe X-ray source ($E_\gamma = 5.9 \text{ keV}$) at the center of the sensitive area, we tested three types of termination: resistive, inductive and capacitive; Fig. 7 shows delay-line output signals for each termination type, on the bottom layer of the anode. In all cases the termination was defined empirically by adjusting its parameters to obtain the best results. For the

resistive termination, we found the best value to be $R_t = 220 \Omega$. The best inductive termination (a coil with wires on a ferrite core [18]) was wound with $n_1 = 7$ turns and $n_2 = 4$ turns. For the capacitive termination, we used $C_t = 68 \text{ pF}$ with a resistor $R_t = 1 \text{ k}\Omega$. One may notice the persistent presence of a bipolar “precursor” signal, preceding the delayed signal. It is due to the capacitive coupling between both anode planes, and it appears at the instance of the electron cloud formation on the last GEM; its 100 ns rise-time corresponds to the drift time of the electrons from the last GEM to the anode [9]. Although the precursor signal is present on both delay-lines, connected to the top and bottom anode strips, it is relatively more pronounced on the bottom one, where the collected charge signal is smaller due to the uneven charge sharing mentioned above. In order to avoid triggering on the precursor pulse, we have finally used a capacitive termination on both delay-lines.

4. Data acquisition system

Fig. 8 shows the CAMAC-based data acquisition scheme. Charge signals from top GEM3 electrode are processed by a charge amplifier (ORTEC⁵ 124, sensitivity = 275 mV pC^{-1}) followed by a shaping timing filter amplifier (TFA); they are digitized by a 12-channels 11-bit integrating analog-to-digital converter (LeCroy⁶—ADC 2249W). The ADC gate pulse is generated by a timer (CAEN⁷ mod 2255B) triggered by the fast signal from the bottom GEM3; it has about 200 ns width, corresponding to the duration of the charge pulse, after the TFA. An electronic logic disables re-triggering of the gate signal for about 120 μs , the time required to perform the conversion in the ADC. The fast signal from the bottom GEM3 electrode is also used as a common ‘START’ signal to the time-to-digital (TDC) CAMAC module (LeCroy—TDC 2228A), which records the time difference between this signal and each of the four ‘STOP’ signals, from each delay-line end-

outputs. All fast signals are processed by current amplifiers (VV44 MPI Heidelberg⁸, 6 ns time constant) and constant fraction discriminators (ORTEC CFD—mod. 934). The data is further routed via a CAMAC crate controller (Sparrow⁹—SCM 301) to the computer, and processed with KmaxNT™ (Sparrow Corporation) software and additional dedicated software for processing and display.

5. System performance

To characterize the performance of the detector we carried out measurements on gain uniformity, energy resolution, differential non-linearity (DNL), integral non-linearity (INL), and spatial resolution of the detector using a ^{55}Fe (5.9 keV) X-ray source and Ar/CO₂ (70/30) gas mixture at atmospheric pressure.

Fig. 9 shows the effective gain as function of VGEM for the 3-GEM detectors. It was measured with a calibrated charge preamplifier, connected to the top (cathode) of GEM3 (Fig. 8). The gain curve for a 2-GEM detector is shown for comparison. We currently work with gain of about 10^5 , which is safer to reach with triple-GEMs [19]. Gain uniformity is demonstrated in Fig. 10, showing energy spectra collected with a collimated source at five different positions over the sensitive area; except from one corner (gas outlet), the detector has a remarkably uniform gain; the energy resolution, $\Delta E/E$, is of 19–20% FWHM, at the gain of 10^5 .

DNL of the position recording was measured by irradiating the entire sensitive area; the X-ray source was positioned 0.7 m away from the window, providing a full detector image with 2048×2048 pixels, Fig. 11. We can notice some defects in the image, corresponding to some defects in the detector, e.g. interrupted anode strips and open connections. For the purpose of DNL evaluation on X and Y coordinates we defined a region of interest (ROI) excluding these

⁵ <http://www.ortec-online.com>

⁶ <http://www.lecroy.com>

⁷ <http://www.caen.it>

⁸ http://www.physi.uni-heidelberg.de/~vwalter/Geraete/VV044_Vorverstaerker/VV44.pdf

⁹ <http://www.sparrowcorp.com/>

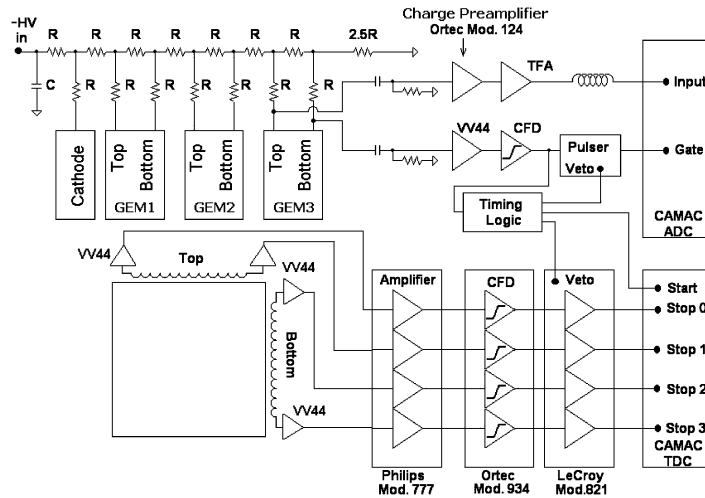


Fig. 8. Electronic diagram showing the power circuit of the GEMs and the CAMAC-based data acquisition setup. All the current amplifiers (VV44) have 6 ns rise-time. In the resistive divider, $R = 22 \text{ M}\Omega$.

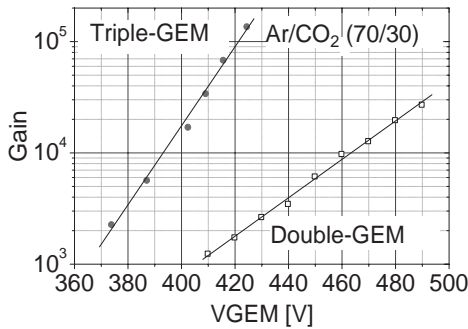


Fig. 9. Effective gain of double- and a triple-GEM detectors as function of the voltage across a GEM, in Ar/CO₂ (70/30) at atmospheric pressure. The signals were recorded with a calibrated charge preamplifier on the top electrode of GEM3.

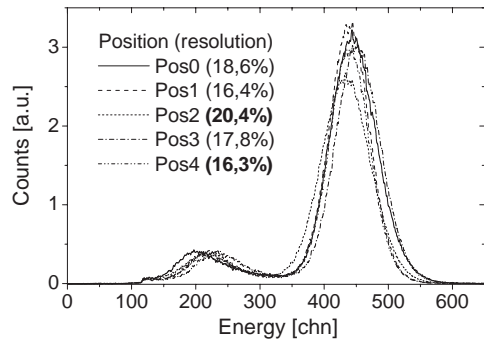


Fig. 10. Energy spectra of 6keV X-rays, recorded at five positions over the sensitive area, Pos0 at the center and Pos1–4 at the four corners. The energy resolution is generally below 20% (FWHM) and the peaks are well above the noise. 1 Atm. Ar/CO₂ (70/30), total gain 10^5 . The signals were recorded on the top electrode of GEM3.

defects and the data from this ROI was projected on the X - and Y -axis; the results are shown in Fig. 12. We define the DNL as the variance of these distributions (RMS); we have measured $DNL_X = 5.1\%$ and $DNL_Y = 5.4\%$. An important component in the DNL originates from the undulating architecture of the delay-line circuit; it introduces a wavy response with peaks spaced by about 130 channels (6.5 mm), which is the undulation pitch (Fig. 2).

The INL in the $X - Y$ response was measured using a laser-trimmed stainless-steel mask, with 20-

slits at 5 mm pitch, each $300 \mu\text{m}$ wide and 15 mm long. The mask was aligned to the anode strips of interest and the detector was irradiated through the slits. Fig. 13a shows a typical image of the mask; Figs. 13b and c show enlarged views of that image aligned to top and bottom anode planes, respectively. The projected image contains peaks, the centroid of which is measured. The INL is the deviation of the measured centroid from a best-fit straight line. The measured centroid positions are shown in Figs. 14a and b as a function of the slit

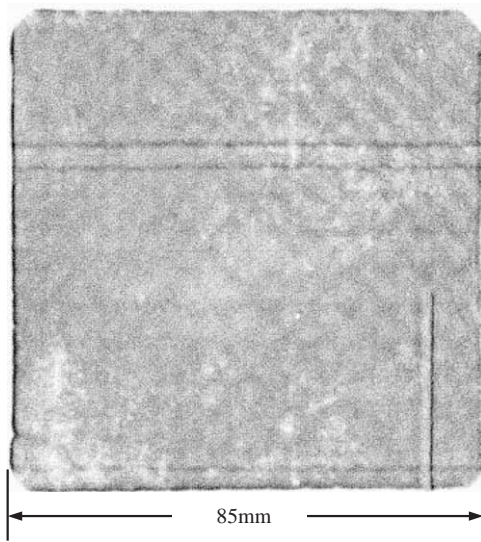


Fig. 11. The 2D response of the detector, under uniform irradiation with an X-ray source positioned 0.7m away from the window. The dark lines on the image are due to broken connections; the short vertical line is due to an interrupted anode strip.

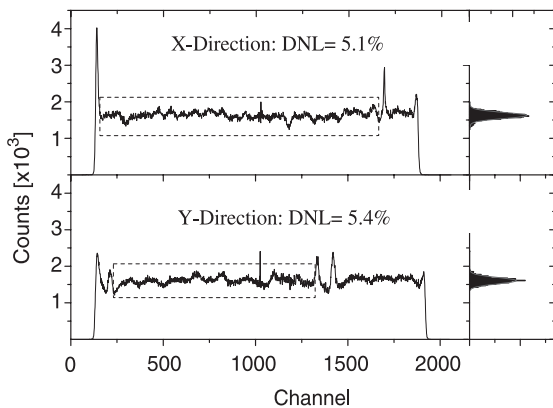


Fig. 12. DNL in the ROI defined on the projected position spectra taken from Fig. 11. The DNL is defined as the variance of the counts distribution for each spectrum.

position; the INL is quoted as a percentage of the full-scale, for top (X) and bottom (Y) anode strip-planes, respectively. We calculated $INL_X \leq 0.12\%$ and $INL_Y \leq 0.15\%$. The undulations on both INL curves are due to the different pitch of the mask slits and the anode strips, resulting in better INL wherever they overlap.

Spatial resolution was measured at five positions over the sensitive area of the detector: Pos0 at the

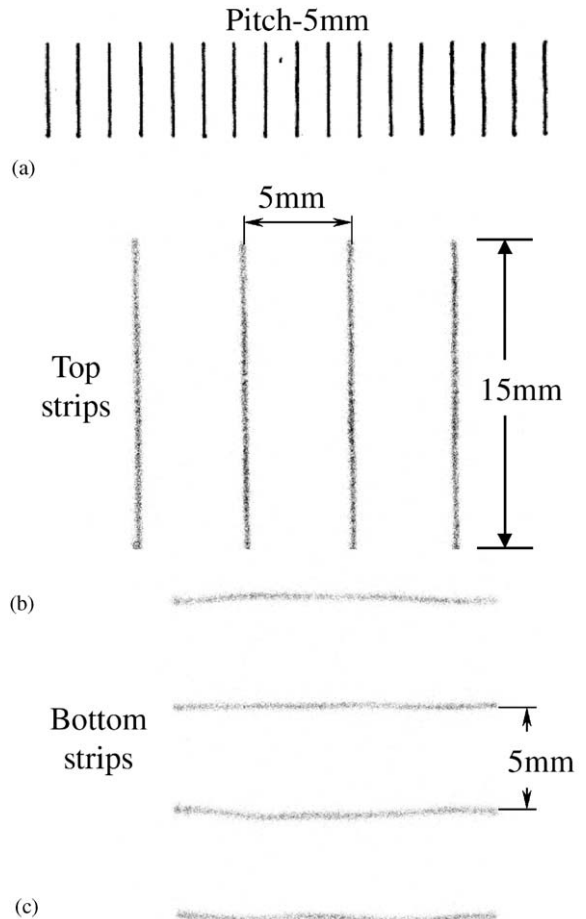


Fig. 13. 2D images recorded with a 20-slits mask of $300\mu\text{m}$ wide, 15 mm long, 5 mm pitch: (a) the full mask; (b) an enlarged segment with the slits parallel to the top (X) anode strips; and (c) same for the bottom (Y) anode strips. The observed non-linearities are discussed in the text.

center and Pos1–4 at each corner. We used a 3-slit collimator with 1.1 mm pitch, 50 mm height and $100\mu\text{m}$ width. The slits were aligned with the top or bottom anode strips to provide the resolution. From the projection of the collimator image on the axis of interest we extracted the rms width of the peaks. Figs. 15a and b show examples of histograms for top (X) and bottom (Y) strip-layers at Pos0, at the center of the detector area. The recorded rms values were corrected for the collimator size and averaged over the three slits to provide the detector's intrinsic resolution (see

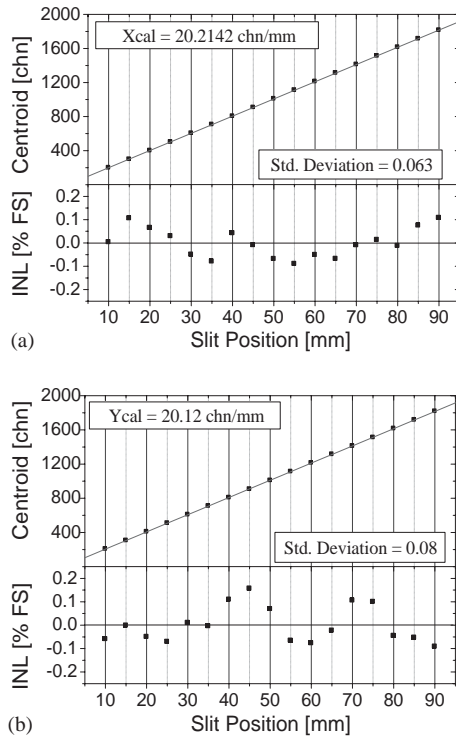
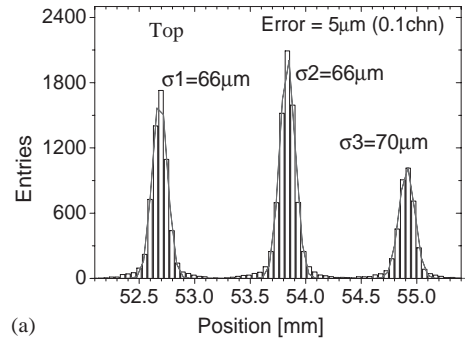


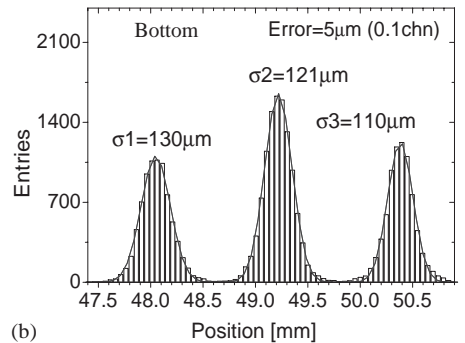
Fig. 14. INL of the detector, calculated from the centroid of peaks in the projected 1D images of the 2D ones shown in Fig. 13. The INL is defined as the maximum deviation of the measured centroid position from its best fit to a straight line.

Table 1). The large spread in the values given in Table 1 is mainly due to the fact that the slit-image width depends on interpolation between the strips; thus, when the collimator slit is positioned in front of a strip, a narrower image is recorded as compared to the case when the slit is between strips.

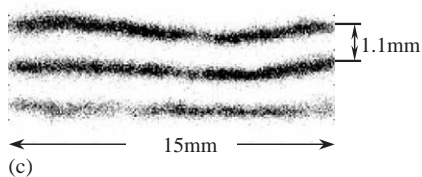
In both top and bottom data set, the worst resolution was recorded at Pos2, where the gas outlet is found and where the delay-line PCBs are closer, which can raise the cross-talk between them and consequently deteriorate the signal. It should also be noted that since the resolution was obtained from a projection of a 50 mm long slit, it contains some contribution from the detector INL, as evident from Fig. 15c, showing the “wavy” 2D slits-image used for the resolution



(a)



(b)



(c)

Fig. 15. Position resolution measured for: (a) top and (b) bottom anode-strip planes recorded at the center of the sensitive area, using a collimator with three slits 50 μm wide and 1 mm apart. The spectra were obtained by projecting the whole 2D image of the 15 mm long slits, shown in (c).

measurements of Fig. 15b (slits aligned to the Y strips).

Fig. 16 illustrates the overall imaging performance of the detector, irradiated through a thin patterned metal mask located at its center. Notice the absence of image defects, generally associated with discharges, indicating upon a very stable operation of the detector. The “wavy” pattern resulting from the INL discussed above can be easily software-corrected.

Table 1

Average values of intrinsic localization resolution, measured at five positions over the detector's sensitive area (Pos0 at the center, Pos1–4 at the corners)

	Pos0	Pos1	Pos2	Pos3	Pos4
Top— σ_X (μm)	54.1	62.4	89.2	78.2	71.0
Bottom— σ_Y (μm)	112.9	113.7	158.9	99.6	91.5

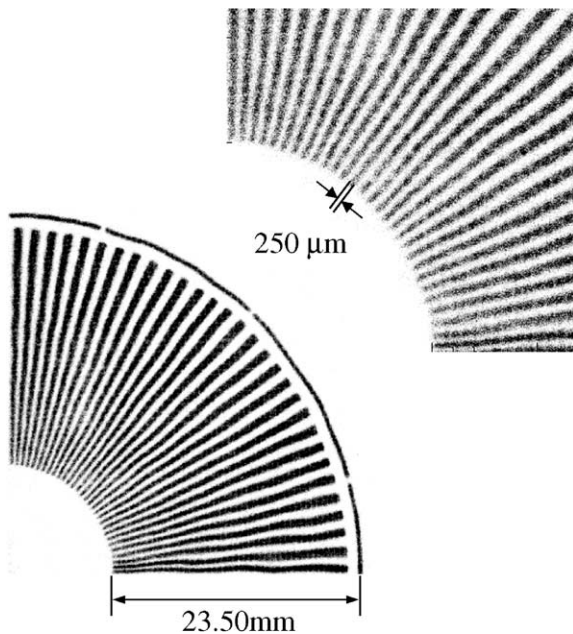


Fig. 16. A 2D X-ray image of a patterned metal mask and a zoom at its center.

6. Summary and discussion

We have investigated the performance of a triple-GEM imaging detector, equipped with a delay-line readout circuit developed within this work. An energy resolution generally below 20% with 6 keV X-rays was recorded, typical for such detectors [13]; a rather uniform gain was found over the detector sensitive area of $100 \times 100 \text{ mm}^2$. We have shown that the delay-line readout can be adapted for position recording with GEM-based radiation detectors, having orthogonal anode strips; the intrinsic spatial resolution is comparable to that obtained with ASIC multi-channel amplifiers [11,13]. This type of economic readout has the

advantages of having very few electronics channels with good position interpolation, good resistance to eventual discharges and rather fast data processing, which depends upon the digitizing electronics. Our demonstration was done with relatively slow electronics, having typical event dead time of $120 \mu\text{s}$ (ADC conversion time). The detector presents a good linearity in its position response; we measured a DNL, of about 5% and an INL, of about 0.15%. The DNL can be easily software-corrected. The average intrinsic spatial resolution over the whole sensitive area is better with the top strips ($\langle \sigma_X \rangle \sim 71 \mu\text{m}$) than with the bottom strips ($\langle \sigma_Y \rangle \sim 115 \mu\text{m}$), due to the uneven charge sharing between the two strip layers. These resolutions are adequate for many radiation imaging applications, e.g. of soft X-rays, thermal neutrons [20], single-photons in gaseous photo-multipliers [21], etc.

Due to the unbalanced charge sharing, the compared performance between top and bottom anode-strip layers is impaired. New studies have been done on the strips geometry in order to balance the charge sharing between top and bottom anode planes and to reduce the parasite capacitance among neighboring strips [7,10,22]. With more adequate 2D strip planes one can improve the position resolution and enhance the AC characteristics of the delay-line leading to better global performance of the detector. We have seen that the discrepancy between the designed and measured delay-line characteristics is mainly due to the anode-strip capacitance and to effects resulting from the architectural design of the delay-line PCB. More careful design of the delay-line circuit architecture would also reduce part of the observed non-linearity.

In this work we have used a discrete-element delay-line, bonded to the anode strips; a more elegant solution consists of 2D readout circuits incorporating both the readout strips and meander delay-lines, on the same PCB [22]. The GEM-induced anode signals have typically narrow distributions [9], necessitating delay-lines with large numbers of cells (small anode-strip pitch). A better solution would consist on measuring charges induced on 2D anode strips, located behind a resistive layer [22,23]; this would yield

broader charge distributions and consequently easier interpolation with larger anode-strip pitch and smaller number of delay-line cells.

Acknowledgements

We are thankful to Dr. F. Sauli, CERN, for supplying us with the GEM detector assembly; we are indebted to Dr. Y. Myasoedov, Dr. M. Rapaport, Y. Gal, Y. Gil, M. Sidi and M. Klin of the Weizmann Institute of Science, for their advice and technical support and to L. Manhaes and H.P. Lima Jr. from CBPF, for their assistance in programming and hardware; G. Guedes thanks CAPES—Brazilian grant agency—for the financial support (PDEE process #2070006) and to the Weizmann Institute of Science for the hospitality during his stay. The present research was partially supported by the Planning and Budgeting Committee of the Council for Higher Education in Israel. A. Breskin is the W. P. Reuther Professor of research in the peaceful use of atomic energy.

References

- [1] F. Sauli, Nucl. Instr. and Meth. A 386 (1997) 531.
- [2] S. Bachmann, A. Bressan, L. Ropelewski, F. Sauli, A. Sharma, D. Mörmann, Nucl. Instr. and Meth. A 438 (1999) 376.
- [3] A. Buzulutskov, A. Breskin, G. Garty, R. Chechik, F. Sauli, L. Shekhtman, Nucl. Instr. and Meth. A 443 (2000) 164; A. Buzulutskov, A. Breskin, G. Garty, R. Chechik, F. Sauli, L. Shekhtman, Nucl. Instr. and Meth. A 442 (2000) 68.
- [4] C. Richter, A. Breskin, R. Chechik, G. Garty, A. Sharma, Nucl. Instr. and Meth. A 478 (2002) 538.
- [5] A. Sharma, Nucl. Instr. and Meth. A 471 (2001) 136.
- [6] D. Mörmann, A. Breskin, R. Chechik, P. Cwetanski, B.K. Singh, Nucl. Instr. and Meth. A 478 (2002) 230.
- [7] S. Kappler, Application of Multi-GEM Detectors in X-ray Imaging, Diploma Thesis, Institut für Experimentelle Kernphysik, Karlsruhe University, Germany, 19 September 2000.
- [8] D. Karlen, et al., Investigation of GEM Space Point Resolution for a TPC Tracker, Proceedings, LCWS 2000 (Physics and Experiments with Future Linear e^+e^- Colliders), Fermilab, October 2000, AIP Conference Proceedings, Vol. 578, 2001, p. 817.
- [9] G.P. Guedes, A. Breskin, R. Chechik, D. Mörmann, Nucl. Instr. Meth. A. 497 (2003) 307.
- [10] S. Bachmann, A. Bressan, B. Ketzer, M. Deutel, L. Ropelewski, F. Sauli, A. Bondar, A. Buzulutskov, L. Shekhtman, A. Sokolov, et al., Nucl. Instr. and Meth. A 470 (2001) 548.
- [11] M. Ziegler, P. Sievers, U. Straumann, Nucl. Instr. and Meth. A 471 (2001) 260.
- [12] Torsten Zeuner, Nucl. Instr. and Meth. A 446 (2000) 324.
- [13] M.C. Altunbas, M. Carpeans, K. Dehmelt, J. Ehlers, J. Friedrich, I. Konorov, A. Gandi, S. Kappler, B. Ketzer, R. de Oliveira, S. Paul, A. Placci, L. Ropelewski, F. Sauli, F. Simon, M. van Stenis, Nucl. Instr. and Meth. A 490 (2002) 177.
- [14] S. Bachmann, S. Kappler, B. Ketzer, Th. Müller, L. Ropelewski, F. Sauli, E. Schulte, Nucl. Instr. and Meth. A 478 (2002) 104.
- [15] A. Bressan, R. De Oliveira, A. Gandi, J.-C. Labbé, L. Ropelewski, F. Sauli, D. Mörmann, T. Müller, H.J. Simonis, Nucl. Instr. and Meth. A 425 (1999) 254.
- [16] M. Overbeck, A. Breskin, M. Brugger, R. Chechik, Z. Fraenkel, G. Hermann, K. Lutzekirchen, S. Polikanov, N. Trautmann, Th. Wilpert, Nucl. Instr. and Meth. A 288 (1990) 413.
- [17] A.F. Barbosa, G.P. Guedes, H.P.L. Júnior, Nucl. Instr. and Meth. A 477 (2002) 41 and references therein.
- [18] M. Birk, A. Breskin, N. Trautner, Nucl. Instr. and Meth. A 137 (1976) 393.
- [19] S. Bachmann, A. Bressan, M. Capeans, M. Deutel, S. Kappler, B. Ketzer, A. Polouektov, L. Ropelewski, F. Sauli, E. Schulte, et al., Nucl. Instr. and Meth. A 479 (2002) 294.
- [20] V. Dangendorf, A. Demian, H. Friedrich, V. Wagner, A. Akkerman, A. Breskin, R. Chechik, A. Gibrekhterman, Nucl. Instr. and Meth. A 350 (1994) 503.
- [21] A. Breskin, T. Boutboul, A. Bouzulutskov, R. Chechik, G. Garty, E. Shefer, B.K. Singh, Nucl. Instr. and Meth. A 442 (2000) 58 and references therein.
- [22] O. Jagutzki, J.S. Lapington, L.B.C. Worth, U. Spillman, V. Mergel, H. Schmidt-Bocking, Nucl. Instr. and Meth. A 477 (2002) 256 and references therein.
- [23] G. Battistoni, et al., Nucl. Instr. and Meth. A 202 (1982) 459.